

Strength enhancement of LiZnVO₄ nanoparticles incorporated with PVDF nanocomposites for high-performance lithium-ion battery application

I. S. Elashmawi (✉ islam_shukri2000@yahoo.com)

National Research Centre, EBehouth St

A. M. Ismail

National Research Centre, EBehouth St

A. M. Abdelghany

National Research Centre, EBehouth St

A. Y. Yassin

Delta University for Science and Technology

Research Article

Keywords: LiZnVO₄ nanoparticles, X-ray Diffraction, FT-IR, UV-Visible, AC electrical modulus

Posted Date: June 23rd, 2022

DOI: <https://doi.org/10.21203/rs.3.rs-1770900/v1>

License:  This work is licensed under a Creative Commons Attribution 4.0 International License.

[Read Full License](#)

Abstract

This work aims to prepare LiZnVO_4 nanoparticles and incorporate them into PVDF as a host polymeric material using the casting method for rechargeable Li-battery applications. The effect of LiZnVO_4 on the structural and optical properties of the samples was studied using XRD, FT-IR, and UV-is techniques. Moreover, the electrical conductivity of the prepared films was studied. The XRD spectra show semicrystalline structure of PVDF and the rhombohedral structure of LiZnVO_4 . Scherer's equation was used to determine the crystallite size of LiZnVO_4 which is nearly 83 nm. The interaction between PVDF and LiZnVO_4 was approved by shifting some FT-IR bands. The band gap energies were decreased by increasing LiZnVO_4 due to the density in the localized states in the mobility band gap in PVDF. The AC parameters as a function of frequency and temperature were investigated in detail. Both ϵ' and ϵ'' had their maximum values at low frequencies and decreased as the frequency and temperature increased. The dielectric properties and $\tan \delta$ were improved, particularly 5 wt% of LiZnVO_4 , which confirms the XRD and FT-IR results indicating their suitability as a suitable base material for designing and developing promising energy storage devices and lithium batteries.

1. Introduction

Modern technology is concerned with the use of lithium-ion polymer batteries as an alternative to the liquid electrolytic battery, which is used as an electrolyte and as a separator [1–4]. This is because the polymeric structure batteries used in the production of batteries greatly help in enhancing safety and security. This is because of the problems that liquid electrolytes come from, such as the decomposition of the liquid and the rise of gases. Generally, polymer film composites are used in lithium batteries for their thermal and electrochemical stability, and good mechanical strength [5–7].

Poly(vinylidene fluoride) (PVDF) is a common polymer host for lithium battery applications [8–10]. PVDF contains a large concentration of charge carriers as a result of the strong electron-withdrawing properties of its functional group ($-\text{C}-\text{F}$) and its high anodic stability. PVDF is receiving great attention for its piezoelectric properties when compared to any other polymer [11]. PVDF is widely used in energy-related applications and specialties. Pure PVDF has many properties such as high chemical resistance, outstanding mechanical strength, piezoelectric, and thermoelectric properties. PVDF is used in many electronic applications and as sheathing for cables used in audio, video, and alarm systems. PVDF is used as a binder for the cathodes and anodes in lithium-ion batteries, and as a battery separator in Li-ion polymer systems [8–17].

Research on materials used as anode confirms that LiZnVO_4 with specific nanoscale sizes can be used in the lithium-ion secondary battery as the negative electrode [18]. The properties of LiZnVO_4 due to its use in lithium storage as it has a high capacity extend by overcharging with high stability in charge and discharge cycles improving the interpretation of secondary Li-ion batteries according to their short diffusion paths and high surface areas [18–20].

At present, polymeric nanomaterials containing nanoparticles are prepared and used, which makes them develop and improve functions within the polymeric matrices [21]. The Li-ion battery technology is an emerging technology for powering microelectronic devices for their large volumetric and power capacities with large progressive life and low discharge rates. Since the reduction of the volume of lithium batteries with liquid electrolytes. Solid-state batteries are an alternative with the availability of easy kinetics of diffusion of Li within the polymer [22–26]. To increase the electrical conductivity of the batteries. This work initially aims to prepare LiZnVO_4 nanoparticles, and then incorporate them in PVDF using the casting method for solid rechargeable battery applications. The effect of LiZnVO_4 on the structural and optical properties within the polymeric matrix is studied using XRD, FT-IR, and UV-is techniques. Moreover, the electrical conductivity properties of the prepared films were studied in detail.

2. Materials And Method

2.1. Materials

PVDF [CH_2CF_2 , $M_w = 543000$] and LiZnVO_4 were provided from Sigma Aldrich. Dimethyl sulfoxide (DMSO) was supplied from the S D Fine-Chem Limited.

2.2. Preparation of PVDF/ LiZnVO_4 composite membranes

At a temperature of 60 °C, 2 gm of PVDF were dissolved in 100 ml DMSO. After that, LiZnVO_4 NPs were added to the solution in increments of 3, 5, and 10 wt. %. then, the suspension was first sonicated to prevent agglomeration in the PVDF solution, and then it was stirred constantly at a temperature of 60 °C until a homogenous solution was created. The resultant solutions were poured onto Petri plates and stored in a vacuum oven at a temperature of 65 °C for approximately 12 hours to remove the solvent. The PVDF/ LiZnVO_4 nanocomposite films were obtained with a thickness of about 20 μm .

2.3. Measurement Techniques

The X-ray diffraction measurements were conducted with a PANalyticalX'Pert Pro operating at 45 KV and employing a Cu-K target with secondary monochromator Holland radiation at $\lambda = 0.1540$ nm with $2\theta = 5-70^\circ$. ATR-FTIR measurements were carried out utilizing a Bruker VERTEX 80 (Germany) combined platinum diamond ATR, which consists of a diamond disc as an internal reflector in the range 4000 – 400 cm^{-1} with a resolution of 4 cm^{-1} and a total of 50 scans. Absorption spectra in the ultraviolet-visible spectrum were examined using a Jasco V-630 UV-VIS (Japan) spectrophotometer. Broadband dielectric spectroscopy (BDS) type (concept 40) novocontrol high-resolution alpha analyzer with Quatro temperature controllers was used to measure AC conductivity.

3. Results And Discussion

3.1. The X-ray diffraction (XRD)

Figure 1 shows the XRD of PVDF and PVDF incorporated with different weight percentages of LiZnVO_4 . PVDF has diffraction peaks at $2\theta = 19.1^\circ, 20.7^\circ$ and 39.7° [27–29]. According to JCPDS Card No. 38-1332, XRD spectrum of LiZnVO_4 shows the rhombohedral structure. Scherer's equation was used to determine the crystallite size of LiZnVO_4 . This equation has the form $C = \frac{K\lambda}{\beta \cos\theta}$, where C is the crystallite size, K is constant equal 0.9 and λ is the X-ray wavelength. θ is the diffraction angle and β is the full width at half maximum of a diffraction peak. For the purpose of computing the mean crystallite size, intense diffraction peaks were chosen, and the result was determined to be 83 nm.

The interaction between PVDF and LiZnVO_4 NPs is confirmed by shifting the diffraction peak of PVDF at $2\theta = 20.7^\circ$ with a variation in its broadening and intensity. The diffraction peaks of LiZnVO_4 begin to appear and their intensities increase with increasing the weight percentage of LiZnVO_4 NPs with shifting in their position that is related to LiZnVO_4 NPs. This indicates the interaction between PVDF and LiZnVO_4 NPs.

3.2. Fourier Transform Infrared (FT-IR)

Figure 2 represents the FT-IR of pure PVDF and PVDF incorporated with different weight percentages of LiZnVO_4 . PVDF exhibits bands at 1402 cm^{-1} and 1071 cm^{-1} which are attributable to the wagging mode of CH_2 [30, 31]. The CF_2 asymmetric stretching vibration is found at 1234 cm^{-1} and 1168 cm^{-1} . The C-C-C asymmetric vibration is observed at 875 cm^{-1} . The CH_2 rocking vibration is visible at 834 cm^{-1} . The CF_2 bending vibrations are shown at 613 cm^{-1} , 510 cm^{-1} and 477 cm^{-1} [27–29]. LiZnVO_4 has bands at 780 cm^{-1} and 710 cm^{-1} which are related to V-O stretching vibration. The band at 414 cm^{-1} is related to the stretching vibration of Zn-O. The stretching vibration of Li- VO_4 is observed at 476 cm^{-1} . The interaction between PVDF and LiZnVO_4 is approved by shifting the band from 834 cm^{-1} to 840 cm^{-1} and shifting the band from 477 cm^{-1} to 471 cm^{-1} with a new band at 409 cm^{-1} .

3.3. Ultraviolet-Visible measurement

Figure 3 shows UV-Visible spectra of pure PVDF and PVDF incorporated with a different weight percentage of LiZnVO_4 in the wavelength range of 190–800 nm. The optical absorption edge can be described using these spectra. All spectra have an intense absorption band at 237 nm. The intensity of this band at 237 nm is increased and the broadening decreases with increasing the weight percentage of LiZnVO_4 which indicated that there is an interaction between PVDF and LiZnVO_4 .

Direct and indirect band gaps are the parameters that categorize polymers with doped fillers. The highest point of the valence band and the lowest point of the conduction band both lie at zero crystal momentum in the case of a direct band gap. Indirect conduction is referred to as conduction in which the bottom of the conduction band does not relate to zero crystal momentum. While in materials with an indirect band gap, the transition from the valence band to the conduction band should be coupled with phonons that have the appropriate magnitude of crystal momentum. Near the fundamental band edge plotting the

relations between $(\alpha h\nu)^2$ and $(\alpha h\nu)^{1/2}$ against photon energy $h\nu$ will allow to determine whether a transition is direct or indirect according to the following relation [32].

$$(\alpha h\nu) = B (h\nu - E_g)^{1/n} \quad (1)$$

where E_g is the band gap energy and B is constant. α is the absorption coefficient calculated from $2.303A/d$ where A is the absorbance and d is the thickness of the prepared films. Plotting α against $h\nu$ gives the value of absorption edge as seen in Fig. 4. n has a different value of 2 or 1/2 according to the type of transition [32–34].

$$(\alpha h\nu) = B (h\nu - E_{gin})^2 \quad (2) \text{ for allowed indirect transition}$$

$$(\alpha h\nu) = B (h\nu - E_{gd})^{1/2} \quad (3) \text{ for allowed direct transition}$$

Figure 5 represents the relation between $(\alpha h\nu)^2$ and $(\alpha h\nu)^{1/2}$ against photon energy $h\nu$. The value of the optical band gap energy can be determined by finding the intercept of the extension of the linear component of these curves to zero absorption on the axis. It is observed that band gap energies are decreased with increasing LiZnVO_4 . New energy levels (traps) have been created between the HOMO and LOMO, which has led to a fall in values. This is a consequence of the formation of disorder. As a result, the density of the localized states in the mobility band gap of the PVDF is increased.

3. 4. Dielectric properties

3.4.1 Dielectric permittivity analysis

As a function of the frequency and temperature, the dielectric behavior of the PVDF polymer filled with different weight percentages of LiZnVO_4 is investigated. The frequency ranged from 0.1 Hz to 7 MHz, and the temperature varied between 30 and 120°C. The following formula is used to represent the real (ϵ') and imaginary (ϵ'') components of the dielectric permittivity [35–38];

$$\epsilon' = \frac{C_e d}{\epsilon_0 A}$$

4

$$\epsilon'' = \frac{\sigma}{2\pi f \epsilon_0}$$

5

where C_e is the capacitance experimentally obtained for a sample under investigation, d is the sample thickness A is the cross-sectional area of the used electrode, and ϵ_0 is the permittivity of free space.

Over the above ranges, Figs. 6 and 7 show the ϵ' and ϵ'' curves as a function of frequency. At low frequencies, both parameters (ϵ' and ϵ'') had their maximum values and began to decrease as the frequency increased. It is clear that both ϵ' and ϵ'' are temperature-dependent parameters since their values have improved as the applied temperature increased.

It is worth mentioning that the high ϵ' values achieved for frequencies lower than 10^2 Hz have been ascribed to the induced dipoles' ability to follow the periodic change in the field direction employed. This alteration is slow; thus, it provides the current dipoles sufficient time to align themselves against/with the applied field direction. This reaction gave rise to a significant increase in interfacial polarization (also known as the Maxwell-Wagner-Sillars polarization), which resulted in the current nanocomposite films having excellent dielectric characteristics.

On the other hand, the substantial drop in the ϵ' values in the high-frequency region was attributed to charge carriers' inability to alter their direction in response to the applied field, leading to the gradual accumulation of ions at the interfacial areas between PVDF and LiZnVO_4 , hence reducing the interfacial polarization. Thus, we can conclude that the minor fluctuations in the ϵ' and ϵ'' values with frequency, seen in Figs. 6 and 7, are owing to the minimal effective impact of ionic polarization combined with the low contribution of electronic polarization. Additionally, this negligible variation is responsible for the dielectric relaxation processes occurring inside the current host matrix [39–41]. So, the introduction of LiZnVO_4 nanofiller into the PVDF host matrix improved the dielectric properties of all samples, particularly the sample with 5 wt% of LiZnVO_4 , which confirms the XRD findings.

The minimum dielectric loss is due to the existence of thin layers of PVDF that function as a protective covering for the Li-ions. This coverage minimizes current leakage caused by direct contact with Li-ions, while also confirming the reasonable compatibility between the LiZnVO_4 and the PVDF matrix. PVDF is a dielectric substance, whereas LiZnVO_4 is a conductive material. Therefore, filling PVDF with the nanofiller resulted in the formation of micro-capacitors inside the current host matrix.

3.4.2. Dielectric relaxation analysis

The variation of loss tangent ($\tan \delta$) of the PVDF/ LiZnVO_4 films as a function of the frequency at 30°C is demonstrated in Fig. 8. A careful examination of this dependency provides a deeper insight into the dielectric relaxation processes occurring inside the PVDF-based system. Loss tangent value is governed by the ratio of dissipated energy (ϵ'') to energy stored (ϵ') by the nanocomposite film under study. This figure is distinguished by the presence of intense relaxation peaks, especially for the samples containing Li-ions at high temperatures. These peaks are attributed to dipolar relaxation responses of the polymeric segments as a consequence of ion-dipole complexation. The appearance of this peak verifies the semicrystalline structure of the PVDF and suggests that ionic conduction dominates within doped with LiZnVO_4 . It has located in the low-frequency region as a result of the α -relaxation process accompanied by the rotational motion of lateral functional groups distributed around the central chain axis inside the polymeric matrix. Further, the observed shift in the peak position toward higher frequencies with

increasing temperature is attributed to the dominance of amorphous regions inside the PVDF host matrix. In other words, the distinct shift in the peak's position towards the high-frequency region indicates that the relaxation time (τ) value decreased as the LiZnVO_4 percentage increased. Thus, the incorporation of conductive lithium ions into the dielectric PVDF produced an interfacial polarization, which resulted from the formation of interfacial areas between the PVDF and the nanofiller. Furthermore, this reduction in the τ value is attributable to the decrease in free volumes within the host matrix upon increasing the LiZnVO_4 concentration giving rise to the accumulation of Li^+ ions in these interfacial regions.

The increase in $\tan \delta$ value with frequency in the low-frequency region is due to the Ohmic elements' dominance over the nanocomposite samples' capacitive nature. $\tan \delta$ increased with increasing frequency and subsequently progressively dropped owing to the increase in capacitive components inside the synthesized samples at 90 and 120°C. This finding leads to shorter relaxation times at higher temperatures, where lithium ions have higher energy. The best value of $\tan \delta$ has attained for the nanocomposite containing 5 wt% of LiZnVO_4 , indicating that the nanofiller was well incorporated into the PVDF, and this confirms the XRD and FT-IR results. This sample shows the greatest improvement in amorphous regions and is recommended for use in the manufacture of lithium solid batteries.

3.4.3. Electric moduli formalism

The electric modulus formalism is mainly used to suppress the contribution of electrode polarization. The dielectric real and imaginary moduli denoted by M' and M'' , respectively were determined by the well-known formulas [42–45]:

$$M' = \frac{\epsilon'}{\epsilon'^2 + \epsilon''^2}$$

6

$$M'' = \frac{\epsilon''}{\epsilon'^2 + \epsilon''^2}$$

7

The dependence of M' values on the frequency at 30°C for the PVDF doped with various concentrations of LiZnVO_4 is exhibited in Fig. 9. The spectra in this figure are characterized by the presence of long-tail lies in the frequency range of 10 Hz – 5 MHz. The presence of such a long tail indicates that the electrode polarization contribution has been completely eliminated. This finding also implies that the PVDF-based nanocomposite films have a remarkable capacitive feature.

The observed reduction in M' values with increasing the LiZnVO_4 contents up to the concentration 5 wt % means that generated ions hop across locations, which indicates that hopping is the dominant conduction mechanism in the current nanocomposite films. The variation of M'' values with frequency

recorded at 30°C for the nanocomposite samples is displayed in Fig. 10. The M'' curves exhibit two distinct loss peaks caused by the migration of induced charge carriers (Li^+ and H^+ ions), implying that the host matrix main chain has been relaxed. The obvious change in the peaks intensities with the increase in the nanofiller percentage refers to the non-Debye behavior of the present nanocomposite films. This change is also largely in agreement with the dielectric relaxation stemming from Maxwell-Wagner-Sillars (MWS) polarization effect. The shift observed in the first characteristic relaxation peak toward the higher frequencies is a good indication of the decrease in relaxation time with the increase of LiZnVO_4 percentage.

The variation of M'' versus M' for the PVDF/ x wt% LiZnVO_4 samples are exhibited in Fig. 11. The Cole-Cole plot is generally divided into three frequency-dependent regions; low, middle, and high-frequency regions. These three regions are ascribed to the grain boundary effect, the participation of grains, and the bulk conduction relaxation process, respectively. The present spectra are characterized by a single semicircular arc attributed to the grain boundary effect and surface polarization, while the observed peak is assigned to the bulk conduction response [38, 46]. The asymmetrical behavior of this relaxation peak verifies the non-Debye dielectric relaxation response. The relaxation peak frequencies are governed by the following equation:

$$f_{\max} \approx \frac{1}{2\pi RC}$$

8

According to this equation, the peak frequency is inversely proportional to the capacitance of the geometrical capacitor. Compared to the observed shift in the f_{\max} toward the lower frequency region, the PVDF/ 5wt% LiZnVO_4 nanocomposite sample has achieved the highest capacitance, recommending it to be used in designing Li-ion batteries. Further, this shift is a clear indication of the small contribution of the grain boundary to the electrical conduction mechanism inside the PVDF host matrix. This performance is attributed to the rotation of the dipoles, which supports the capacitive nature of the present nanocomposite film on resistive behavior and gives it valuable comparative advantages over other composites.

3.5. Electrical conduction behavior

Figure 12 shows the dependency of AC conductivity (σ_{ac}) on frequency for the above-described nanocomposite samples recorded at 30°C. As the concentration of LiZnVO_4 increased, amorphous areas became more dominant over crystalline regions, thus facilitating the transit of induced ions over short-range distances, giving rise to the detected increase in σ_{ac} values. The relaxation of ions via bouncing back and forth across localized sites increased with increasing frequency, resulting in the enhancement of electrical conductivity. This improvement is attributed to the shift in hopping behavior from long-range to short-range distances.

The σ_{ac} curves have been divided into three main parts; the first part located in the low-frequency region (region I) represents the DC conductivity (σ_{dc}), whereas the second part (region II) reveals the dispersive region and is located at 100 Hz – 5 MHz. The third segment (region III) is located at $f < 5$ MHz, where the induced ions cannot follow the rapid rotation of the direction of the applied field, forming ion-pairs and ion-triplets, which affects their mobility and thus reduces the AC conductivity at this stage.

The three parts of σ_{ac} curves can be elucidated using the jump relaxation model. This model is based on the ratio between successful hops getting back to their original site to unsuccessful hops (i.e., it gets back to their original site). The variation in this ratio between successful and unsuccessful hops has resulted in the observed difference in the σ_{ac} values over the considered range of frequency for the PVDF-based nanocomposite samples. Thus, the universal power-law set by Jonscher is the relevant law for describing the electrical conduction in the nanocomposite samples, and is represented as follows [37, 39, 40];

$$\sigma = \sigma_{dc} + A\omega^S$$

9

where A is a factor that depends on temperature. S is a frequency exponent, which affects by the translational movement of the induced ions during the electrical conduction process inside the PVDF/LiZnVO₄ nanocomposite samples.

The variation of σ_{ac} with frequency curves of the sample containing 5 wt% of LiZnVO₄ (the optimized percentage) at different temperatures is demonstrated in Fig. 13. Similar behavior has been reported in the literature. This figure shows that as the temperature applied to the sample increases, so the σ_{ac} values, emphasizing the thermally activated behavior of the induced ions inside the nanocomposite matrix. The behavior of S values for the PVDF/5% LiZnVO₄ sample studied in the temperature range 30°C-120°C is exhibited in Fig. 14, where a decrease in S values with the continuous increase in temperature is observed. This result indicates that the most appropriate model for elucidating and describing the behavior of ions during the conduction process inside the current nanocomposite samples is the correlated barrier hopping model, confirming the above findings. According to Laumann et al. research, these results may be ascribed to the low-temperature diffusion of lithium ions mainly through the path Li (8a) → V(16c) → V(8a), where these sites are thought to be metastable for the migration of lithium ions. These findings reveal that the studied films filled with LiZnVO₄ have advantageous features, indicating their suitability as a qualified base material for designing and developing promising energy storage devices and lithium batteries.

4. Conclusion

This research extracted the preparation and characterization of LiZnVO₄ nanoparticles as a new nanomaterial. The prepared LiZnVO₄ was combined with PVDF as a basic polymeric material whose properties need to be modified and improved for possible use in solid lithium battery applications. The

structural, optical, and electrical properties of PVDF/LiZnVO₄ nanocomposites were studied. The characteristic X-ray diffraction peaks of PVDF and LiZnVO₄ were observed. The XRD spectra show the rhombohedral structure of LiZnVO₄. Scherer's equation was used to determine the crystallite size of LiZnVO₄ and the result was determined to be 83 nm. The main characteristic IR bands of PVDF as a host material were detected. An interaction between PVDF and LiZnVO₄ was approved by shifting some IR bands. The behaviour of the energy band gap was decreased with increasing LiZnVO₄ due to the formation of disorder and the density of the localized states in the mobility band gaps. The dielectric behavior as a function of frequency and temperature of the PVDF/LiZnVO₄ was investigated. At the lower range of the frequencies, both ϵ' and ϵ'' had their maximum values and began to decrease as the frequency and temperature increased. The cole-cole plots were divided into three frequency-dependent regions (low, middle, and high-frequency) which ascribed to the grain boundary effect, the participation of grains, and the bulk conduction relaxation process, respectively. The spectra were characterized by a semicircular arc attributed to the grain boundary effect and surface polarization, while the spike observed is assigned to the bulk conduction response. The Jonscher universal power law was relevant law to describe the electrical conduction in the prepared samples indicating their suitability as a qualified base material for designing and developing promising energy storage devices and lithium batteries.

Declarations

Funding declaration:

The authors received no financial support for the research, authorship, and/or publication of this article.

Conflicts of interest:

The authors declared that they have no conflict of interest.

Author contributions:

I. S. Elashmawi: supervised the findings of this work, writing - original draft, review and Editing. **A. M. Ismail:** contributed to sample preparation, formal Analysis, investigation, writing-original draft **A. M. Abdelghany:** conceived of the presented idea, carried out the experiment with A. M. Ismail, analysis, review, **A.Y. Yassin:** investigation, derived the models and analyzed the data of AC conductivity, writing - original draft, review. All authors discussed the results and contributed to the final manuscript.

References

1. A. Yoshino, The birth of the lithium-ion battery, *Angew. Chemie - Int. Ed.* 51 (2012) 5798–5800. <https://doi.org/10.1002/anie.201105006>.
2. H.S. Choe, J. Giaccai, M. Alamgir, K.M. Abraham, Preparation and characterization of poly(vinyl sulfone)- and poly(vinylidene fluoride)-based electrolytes, *Electrochim. Acta.* 40 (1995) 2289–2293.

[https://doi.org/10.1016/0013-4686\(95\)00180-M](https://doi.org/10.1016/0013-4686(95)00180-M).

3. G.B. Appetecchi, F. Croce, B. Scrosati, High-performance electrolyte membranes for plastic lithium batteries, *J. Power Sources*. 66 (1997) 77–82. [https://doi.org/10.1016/S0378-7753\(96\)02484-6](https://doi.org/10.1016/S0378-7753(96)02484-6).
4. J.Y. Song, Y.Y. Wang, C.C. Wan, - Open Access Library Song, J.Y.; Wang, Y.Y.; Wan, C.C. Review of gel-type polymer electrolytes for lithium-ion batteries. *J. Power Sources* 1999, 77, 183–197, doi:10.1016/S0378-7753(98)00193-1., *J. Power Sources*. 77 (1999) 183–197. <http://www.oalib.com/references/9023829>.
5. A.M. Stephan, Review on gel polymer electrolytes for lithium batteries, *Eur. Polym. J.* 42 (2006) 21–42. <https://doi.org/10.1016/j.eurpolymj.2005.09.017>.
6. X. Bai, T. Li, Z. Dang, Y.X. Qi, N. Lun, Y.J. Bai, Ionic conductor of Li₂SiO₃ as an effective dual-functional modifier to optimize the electrochemical performance of Li₄Ti₅O₁₂ for high-performance Li-ion batteries, *ACS Appl. Mater. Interfaces*. 9 (2017) 1426–1436. <https://doi.org/10.1021/acsami.6b10795>.
7. J. Lu, Z. Chen, Z. Ma, F. Pan, L.A. Curtiss, K. Amine, The role of nanotechnology in the development of battery materials for electric vehicles, *Nat. Nanotechnol.* 11 (2016) 1031–1038. <https://doi.org/10.1038/nnano.2016.207>.
8. I.S. Elashmawi, L.H. Gaabour, Raman, morphology and electrical behavior of nanocomposites based on PEO/PVDF with multi-walled carbon nanotubes, *Results Phys.* 5 (2015) 105–110. <https://doi.org/10.1016/j.rinp.2015.04.005>.
9. M. Mohseni, A.R. Ahmad, F. H Shirazi, N.H. Nemati, Preparation and characterization of self-electrical stimuli conductive gellan based nano scaffold for nerve regeneration containing chopped short spun nanofibers of PVDF/MCM41 and polyaniline/graphene nanoparticles: Physical, mechanical and morphological studies, *Int. J. Biol. Macromol.* 167 (2021) 881–893. <https://doi.org/10.1016/j.ijbiomac.2020.11.045>.
10. Z. Gao, S. Zhang, Z. Huang, Y. Lu, W. Wang, K. Wang, J. Li, Y. Zhou, L. Huang, S. Sun, Protection of Li metal anode by surface-coating of PVDF thin film to enhance the cycling performance of Li batteries, *Chinese Chem. Lett.* 30 (2019) 525–528. <https://doi.org/10.1016/j.ccllet.2018.05.016>.
11. Y.P. Su, L.N. Sim, X. Li, H.G.L. Coster, T.H. Chong, Anti-fouling piezoelectric PVDF membrane: Effect of morphology on dielectric and piezoelectric properties, *J. Memb. Sci.* 620 (2021) 118818. <https://doi.org/10.1016/j.memsci.2020.118818>.
12. X. Zhao, C. Li, R. Qi, H. Guo, G. Peng, Study on relaxation behavior of all-polymer PVDF-based films containing dielectric fluoroelastomer, *Polymer (Guildf)*. 252 (2022) 1–9. <https://doi.org/10.1016/j.polymer.2022.124933>.
13. Y.P. Su, L.N. Sim, H.G.L. Coster, T.H. Chong, Incorporation of barium titanate nanoparticles in piezoelectric PVDF membrane, *J. Memb. Sci.* 640 (2021) 119861. <https://doi.org/10.1016/j.memsci.2021.119861>.
14. B.P.S. Santos, J.J.R. Arias, F.E. Jorge, R.É.P.D. Santos, B.S. Fernandes, L.S. Candido, A.C.C. Peres, G. Chaves, M.F.V. Marques, PVDF containing different oxide nanoparticles for application in oil and gas

- pipelines, *Mater. Today Commun.* 26 (2021) 101743.
<https://doi.org/10.1016/j.mtcomm.2020.101743>.
15. Y.K. Kim, S.H. Hwang, H.J. Seo, S.M. Jeong, S.K. Lim, Effects of biomimetic cross-sectional morphology on the piezoelectric properties of BaTiO₃ nanorods-contained PVDF fibers, *Nano Energy*. 97 (2022) 107216. <https://doi.org/10.1016/j.nanoen.2022.107216>.
 16. Q. Ye, H. Liang, S. Wang, C. Cui, C. Zeng, T. Zhai, H. Li, Fabricating a PVDF skin for PEO-based SPE to stabilize the interface both at cathode and anode for Li-ion batteries, *J. Energy Chem.* 70 (2022) 356–362. <https://doi.org/10.1016/j.jechem.2022.02.037>.
 17. H. Widiyandari, O. Ade Putra, A. Purwanto, Z. Abidin, Synthesis of PVDF/SiO₂ nanofiber membrane using electrospinning method as a Li-ion battery separator, *Mater. Today Proc.* 44 (2020) 3245–3248. <https://doi.org/10.1016/j.matpr.2020.11.448>.
 18. J. Wang, Q. Deng, M. Li, K. Jiang, Z. Hu, J. Chu, High-capacity and long-life lithium storage boosted by pseudocapacitance in three-dimensional MnO-Cu-CNT/graphene anodes, *Nanoscale*. 10 (2018) 2944–2954. <https://doi.org/10.1039/c7nr08191j>.
 19. B.K. Grandhe, S. Ramaprabhu, S. Buddhudu, K. Sivaiah, V.R. Bandi, K. Jang, Spectral characterization of novel LiZnVO₄ phosphor, *Opt. Commun.* 285 (2012) 1194–1198.
<https://doi.org/10.1016/j.optcom.2011.10.013>.
 20. M. Ram, Structure and electrical conduction behavior of LiZnVO₄ ceramic prepared by solution-based chemical route, *J. Alloys Compd.* 509 (2011) 5688–5691.
<https://doi.org/10.1016/j.jallcom.2011.02.128>.
 21. I.S. Elashmawi, N.S. Alatawi, N.H. Elsayed, Preparation and characterization of polymer nanocomposites based on PVDF/PVC doped with graphene nanoparticles, *Results Phys.* 7 (2017) 636–640. <https://doi.org/10.1016/j.rinp.2017.01.022>.
 22. W. Tuichai, A. Karaphun, C. Ruttanapun, Improved dielectric properties of PVDF polymer composites filled with Ag nanomaterial deposited reduced graphene oxide (rGO) hybrid particles, *Mater. Res. Bull.* 145 (2022) 111552. <https://doi.org/10.1016/j.materresbull.2021.111552>.
 23. M. Sato, H. Ishii, Y. Sueda, K. Watanabe, D. Nagao, A reinforced, high-κ ternary polymer nanocomposite dielectrics of PVDF, barium titanate nanoparticles, and TEMPO-oxidized cellulose nanofibers, *Compos. Part C Open Access*. 5 (2021) 100163.
<https://doi.org/10.1016/j.jcomc.2021.100163>.
 24. B. K, A.B. Gueye, D. Rouxel, N. Kalarikkal, S. Thomas, Lithium-ion battery separators based on electrospun PVDF: A review, *Surfaces and Interfaces*. 31 (2022) 101977.
<https://doi.org/10.1016/j.surfin.2022.101977>.
 25. Y. Wang, K. Huang, P. Zhang, H. Li, H. Mi, PVDF-HFP based polymer electrolytes with high Li⁺ transference number enhancing the cycling performance and rate capability of lithium metal batteries, *Appl. Surf. Sci.* 574 (2022) 151593. <https://doi.org/10.1016/j.apsusc.2021.151593>.
 26. A.A. Menazea, A.M. Ismail, I.S. Elashmawi, The role of Li₄Ti₅O₁₂ nanoparticles on enhancement the performance of PVDF/PVK blend for lithium-ion batteries, *J. Mater. Res. Technol.* 9 (2020) 5689–

5698. <https://doi.org/10.1016/j.jmrt.2020.03.093>.
27. I.S. Elashmawi, Effect of LiCl filler on the structure and morphology of PVDF films, *Mater. Chem. Phys.* 107 (2008) 96–100. <https://doi.org/10.1016/j.matchemphys.2007.06.045>.
28. I.S. Elashmawi, E.M. Abdelrazek, H.M. Ragab, N.A. Hakeem, Structural, optical and dielectric behavior of PVDF films filled with different concentrations of iodine, *Phys. B Condens. Matter.* 405 (2010). <https://doi.org/10.1016/j.physb.2009.08.037>.
29. I.S. Elashmawi, A.A. Al-Muntaser, A.M. Ismail, Structural, optical, and dielectric modulus properties of PEO/PVA blend filled with metakaolin, *Opt. Mater. (Amst).* 126 (2022) 112220. <https://doi.org/10.1016/j.optmat.2022.112220>.
30. I.S. Elashmawi, N.H. Elsayed, F.A. Altalhi, The changes of spectroscopic, thermal and electrical properties of PVDF/PEO containing lithium nanoparticles, *J. Alloys Compd.* 617 (2014) 877–883. <https://doi.org/10.1016/j.jallcom.2014.08.088>.
31. E.M. Abdelrazek, I.S. Elashmawi, H.M. Ragab, Manifestation of MnCl₂ fillers incorporated into the polymer matrices in their dielectric properties, *Phys. B Condens. Matter.* 403 (2008) 3097–3104. <https://doi.org/10.1016/j.physb.2008.03.012>.
32. A.A. Menazea, E. Alzahrani, A.A. Shaltout, Gamma radiation introduces improvement in AC conductivity behavior and dielectric characterization of CuONPs @ PVP - PVA nano matrix films prepared by one - potential laser ablation method, (2022).
33. S.A. Nouh, K. Benthami, Gamma induced changes in the structure and optical properties of ZnS/PVA nanocomposite, *J. Vinyl Addit. Technol.* 25 (2019) 271–277. <https://doi.org/10.1002/vnl.21689>.
34. K.I. Hussein, A.Z. Alzuhair, M.S. Alqahtani, A.A. Meshawi, R.Z. Alhifzi, I.S. Yahia, H.Y. Zahran, F.F. Alqahtani, M. Reben, E.S. Yousef, Optical properties and novelty preparation PVA/PVP doping with Cu as surface plasmonic ions, *Optik (Stuttg).* 259 (2022) 168965. <https://doi.org/10.1016/j.ijleo.2022.168965>.
35. A.Y. Yassin, A.R. Mohamed, A.M. Abdelghany, E.M. Abdelrazek, Enhancement of dielectric properties and AC electrical conductivity of nanocomposite using poly (vinyl chloride-co-vinyl acetate-co-2-hydroxypropyl acrylate) filled with graphene oxide, *J. Mater. Sci. Mater. Electron.* 29 (2018) 15931–15945. <https://doi.org/10.1007/s10854-018-9679-7>.
36. J. Zhu, H. Gu, Z. Luo, N. Haldolaarachige, D.P. Young, S. Wei, Z. Guo, Carbon nanostructure-derived polyaniline metacomposites: Electrical, dielectric, and giant magnetoresistive properties, *Langmuir.* 28 (2012) 10246–10255. <https://doi.org/10.1021/la302031f>.
37. A.Y. Yassin, Dielectric spectroscopy characterization of relaxation in composite based on (PVA–PVP) blend for nickel–cadmium batteries, *J. Mater. Sci. Mater. Electron.* 31 (2020) 19447–19463. <https://doi.org/10.1007/s10854-020-04478-1>.
38. A.Y. Yassin, Impedance, structural and thermal analyses of polyvinyl alcohol/polyvinyl pyrrolidone blend incorporated with Li⁺ ions for lithium-ion batteries, *J. Mater. Res. Technol.* 15 (2021) 754–767. <https://doi.org/10.1016/j.jmrt.2021.08.063>.

39. A. Arya, A.L. Sharma, Effect of salt concentration on dielectric properties of Li-ion conducting blend polymer electrolytes, *J. Mater. Sci. Mater. Electron.* 29 (2018) 17903–17920.
<https://doi.org/10.1007/s10854-018-9905-3>.
40. Z. Wang, W. Zhou, L. Dong, X. Sui, H. Cai, J. Zuo, Q. Chen, Dielectric spectroscopy characterization of relaxation process in Ni/epoxy composites, *J. Alloys Compd.* 682 (2016) 738–745.
<https://doi.org/10.1016/j.jallcom.2016.05.025>.
41. V. Siva, D. Vanitha, A. Murugan, A. Shameem, S.A. Bahadur, Studies on structural and dielectric behaviour of PVA/PVP/SnO nanocomposites, *Compos. Commun.* 23 (2021) 100597.
<https://doi.org/10.1016/j.coco.2020.100597>.
42. A. Bettaibi, R. Jemai, M.A. Wederni, R. M'Nassri, M. Barbouche, H. Rahmouni, K. Khirouni, Effect of erbium concentration on the structural, optical and electrical properties of a Bi₄Ti₃O₁₂ system, *RSC Adv.* 7 (2017) 22578–22586. <https://doi.org/10.1039/c6ra27906f>.
43. A.A.A. Youssef, The Permittivity and AC Conductivity of the Layered Perovskite [(CH₃)(C₆H₅)₃P]₂HgI₄, *Zeitschrift Fur Naturforsch. - Sect. A J. Phys. Sci.* 57 (2002) 263–269.
<https://doi.org/10.1515/zna-2002-0510>.
44. S. Ren, J. Liu, D. Wang, J. Zhang, X. Ma, M. Knapp, L. Liu, H. Ehrenberg, Dielectric relaxation behavior induced by lithium migration in Li₄Ti₅O₁₂ spinel, *J. Alloys Compd.* 793 (2019) 678–685.
<https://doi.org/10.1016/j.jallcom.2019.04.216>.
45. A.Y. Yassin, A.M. Abdelghany, Synthesis and thermal stability, electrical conductivity and dielectric spectroscopic studies of poly (ethylene-co-vinyl alcohol)/graphene oxide nanocomposite, *Phys. B Condens. Matter.* 608 (2021). <https://doi.org/10.1016/j.physb.2020.412730>.
46. I.S. Elashmawi, A.M. Ismail, Study of the spectroscopic, magnetic, and electrical behavior of PVDF/PEO blend incorporated with nickel ferrite (NiFe₂O₄) nanoparticles, *Polym. Bull.* (2022).
<https://doi.org/10.1007/s00289-022-04139-9>.

Figures

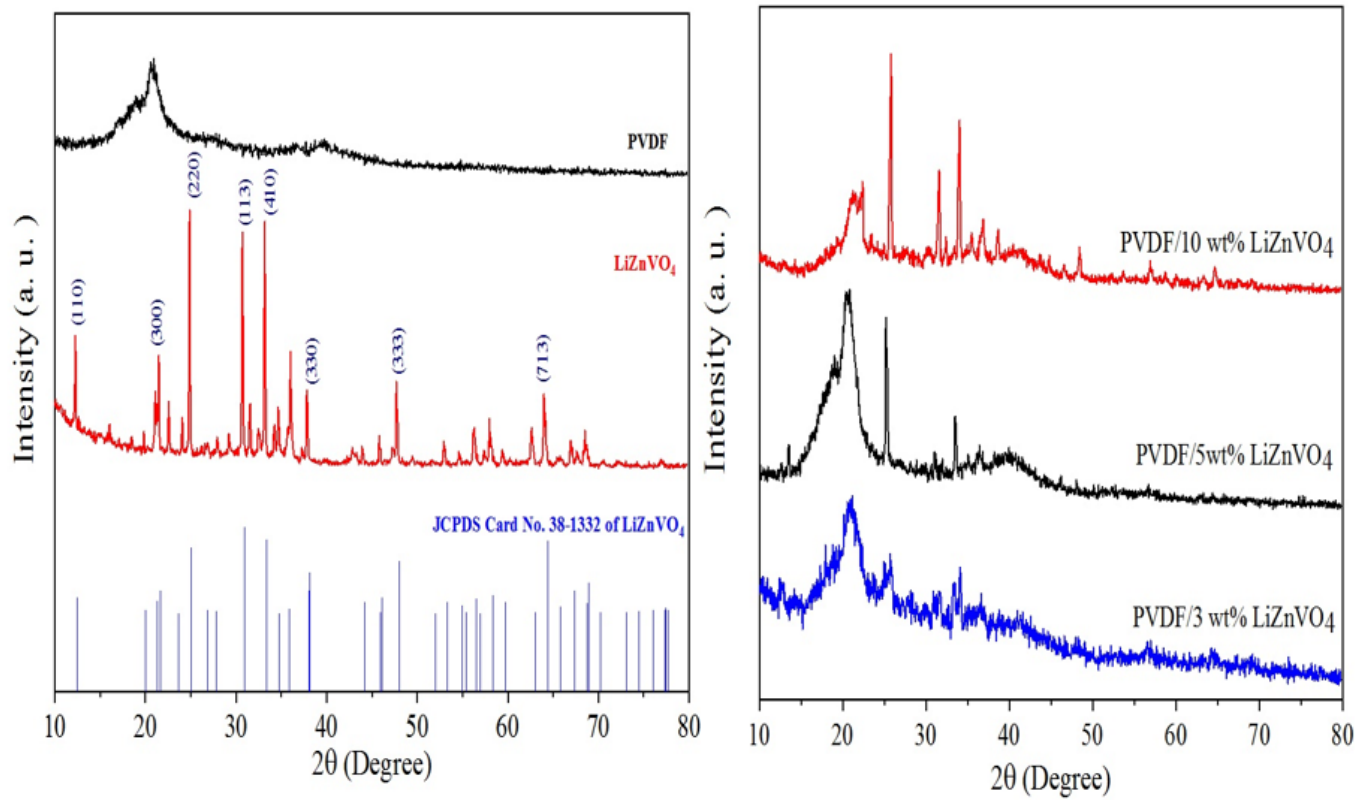


Figure 1

XRD of PVDF and PVDF doped with a different weight percentage of LiZnVO₄.

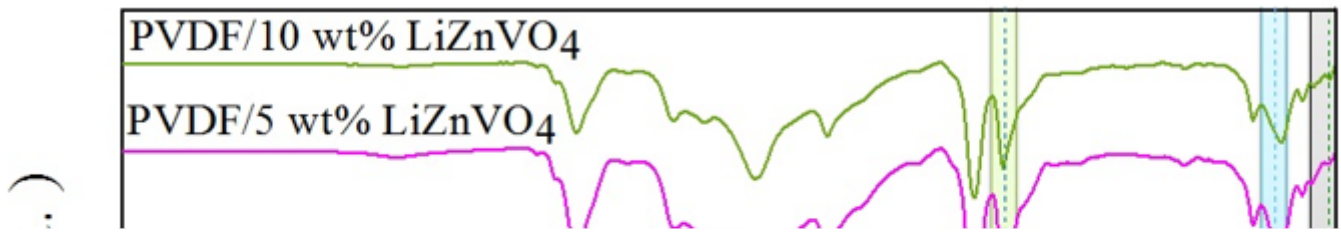


Figure 2

FTIR of PVDF and PVDF doped with a different weight percentage of LiZnVO₄.

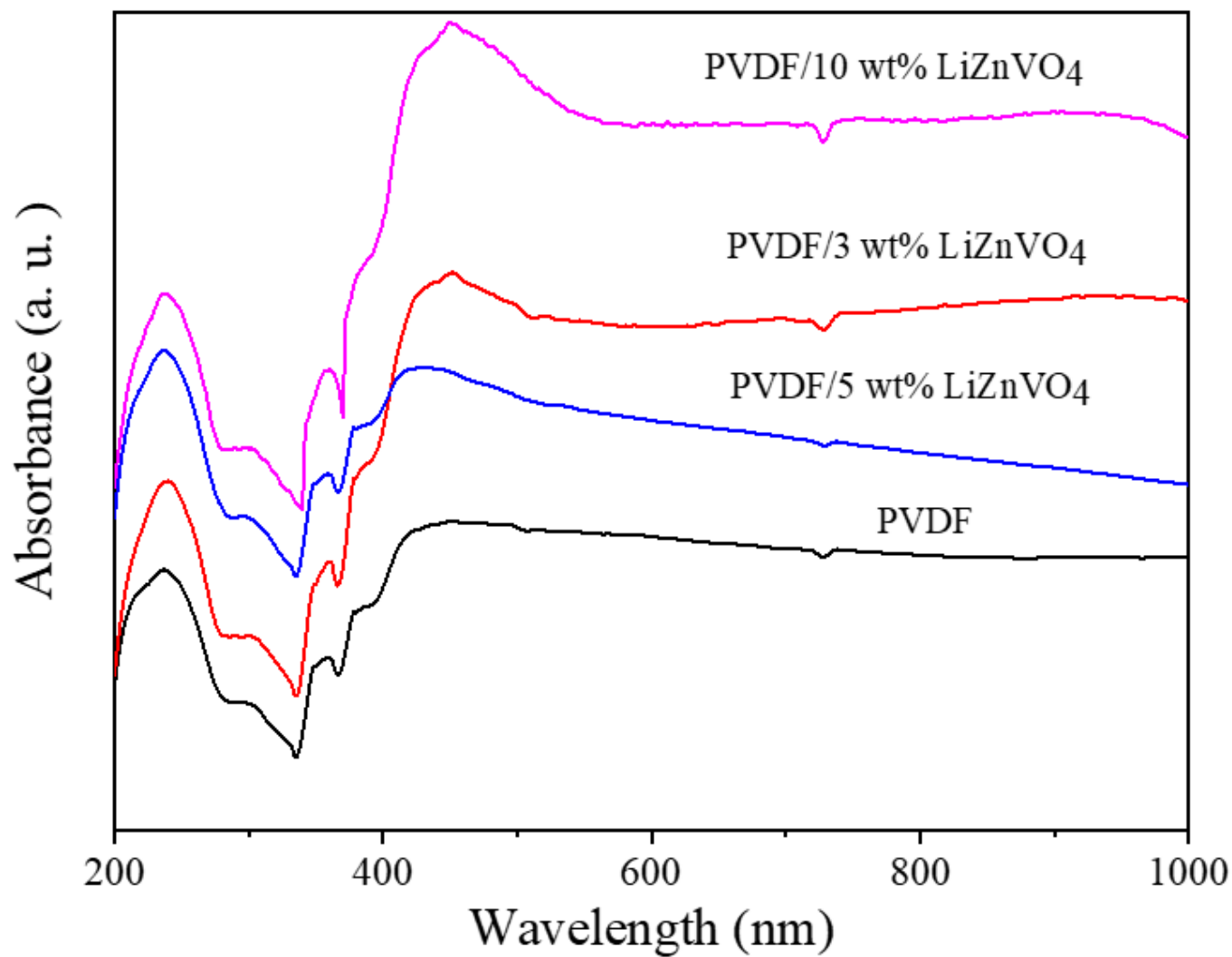


Figure 3

UV-Vis spectra of PVDF and PVDF doped with a different weight percentage of LiZnVO₄.

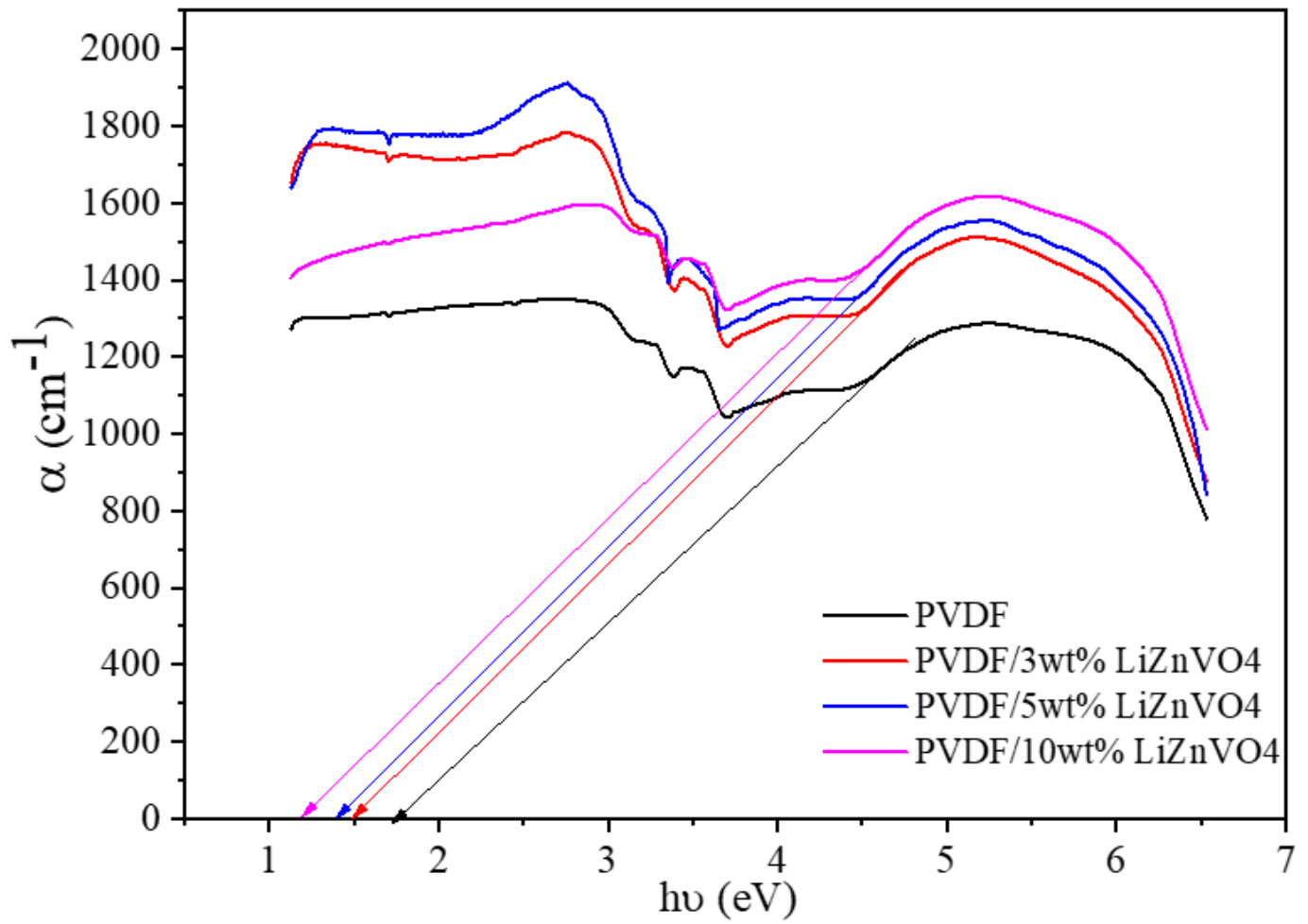


Figure 4

Relation between absorption coefficient against photon energy of PVDF and PVDF doped with a different weight percentage of LiZnVO₄.

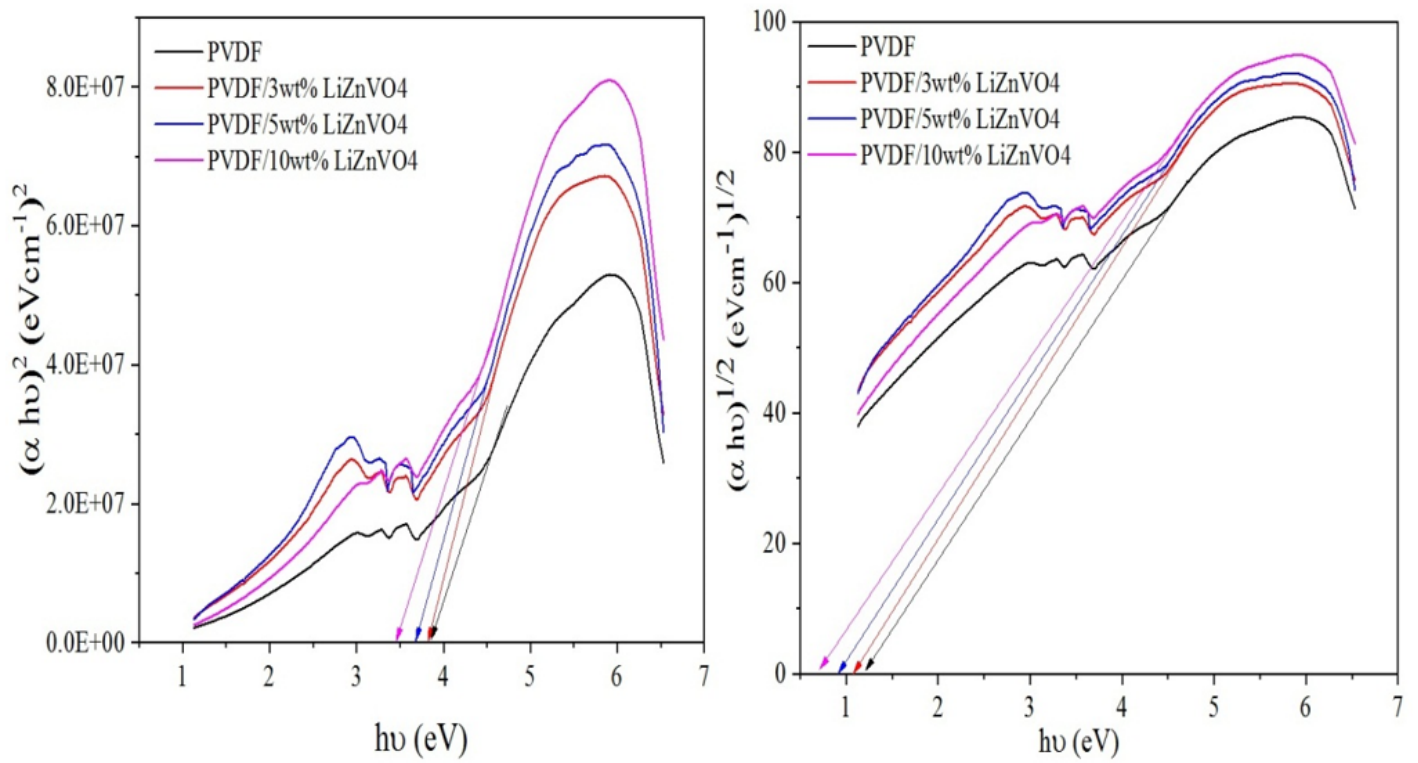


Figure 5

Relation between $(\alpha h\nu)^2$ and $(\alpha h\nu)^{1/2}$ against photon energy of PVDF and PVDF doped with a different weight percentage of LiZnVO₄.

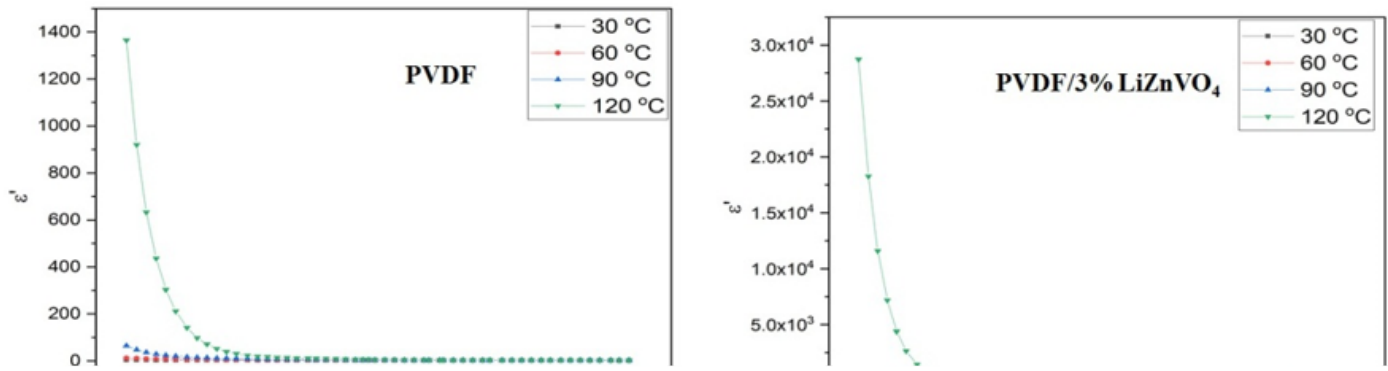


Figure 6

The ϵ' curves of PVDF and PVDF doped with a different weight percentage of LiZnVO_4 samples as a function of frequency and temperature.

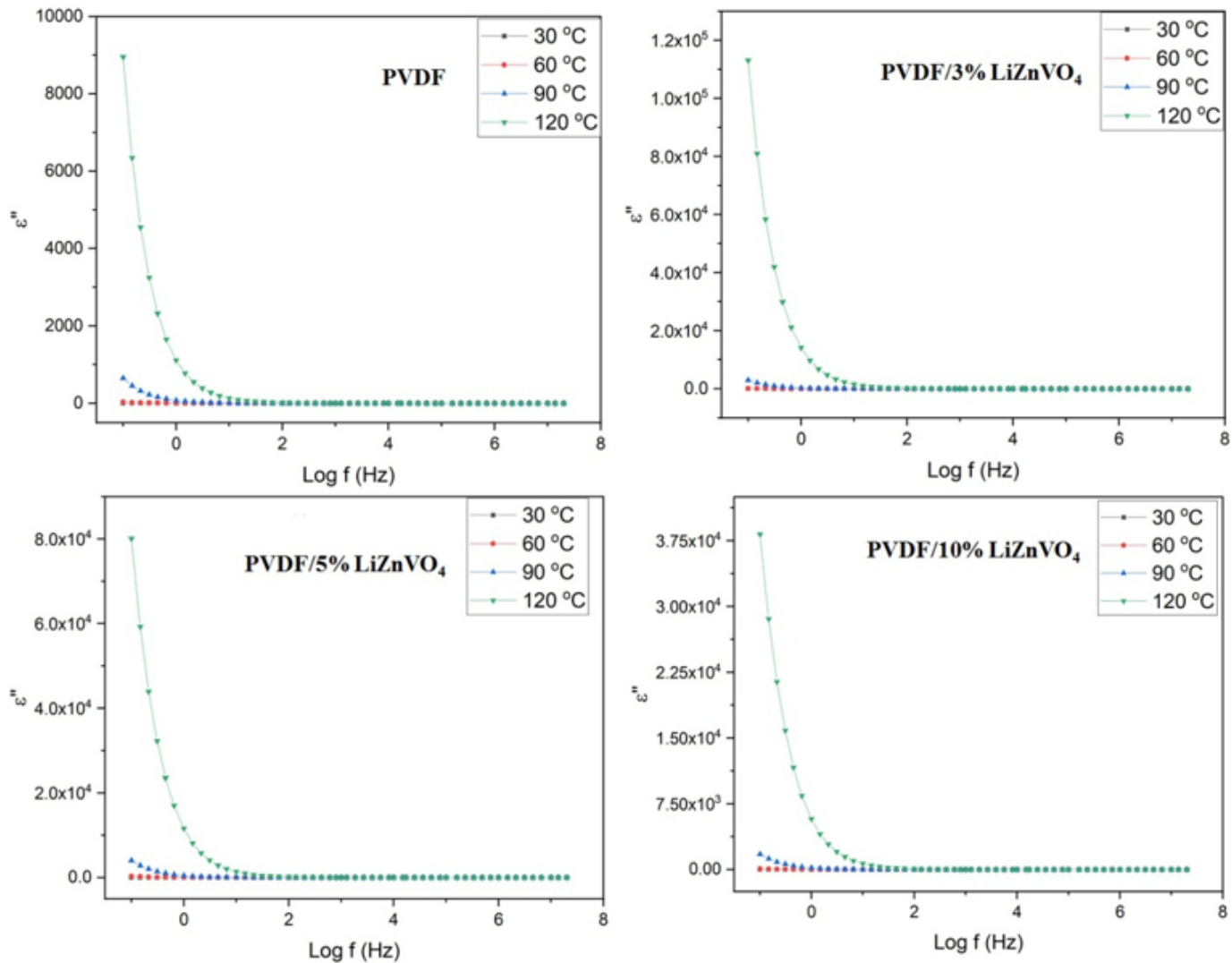


Figure 7

The ϵ'' curves of PVDF and PVDF doped with a different weight percentage of LiZnVO_4 samples as a function of frequency and temperature.

Figure 8

The variation of loss tangent ($\tan d$) with frequency at 30 °C of PVDF and PVDF doped with a different weight percentage of LiZnVO_4 samples.

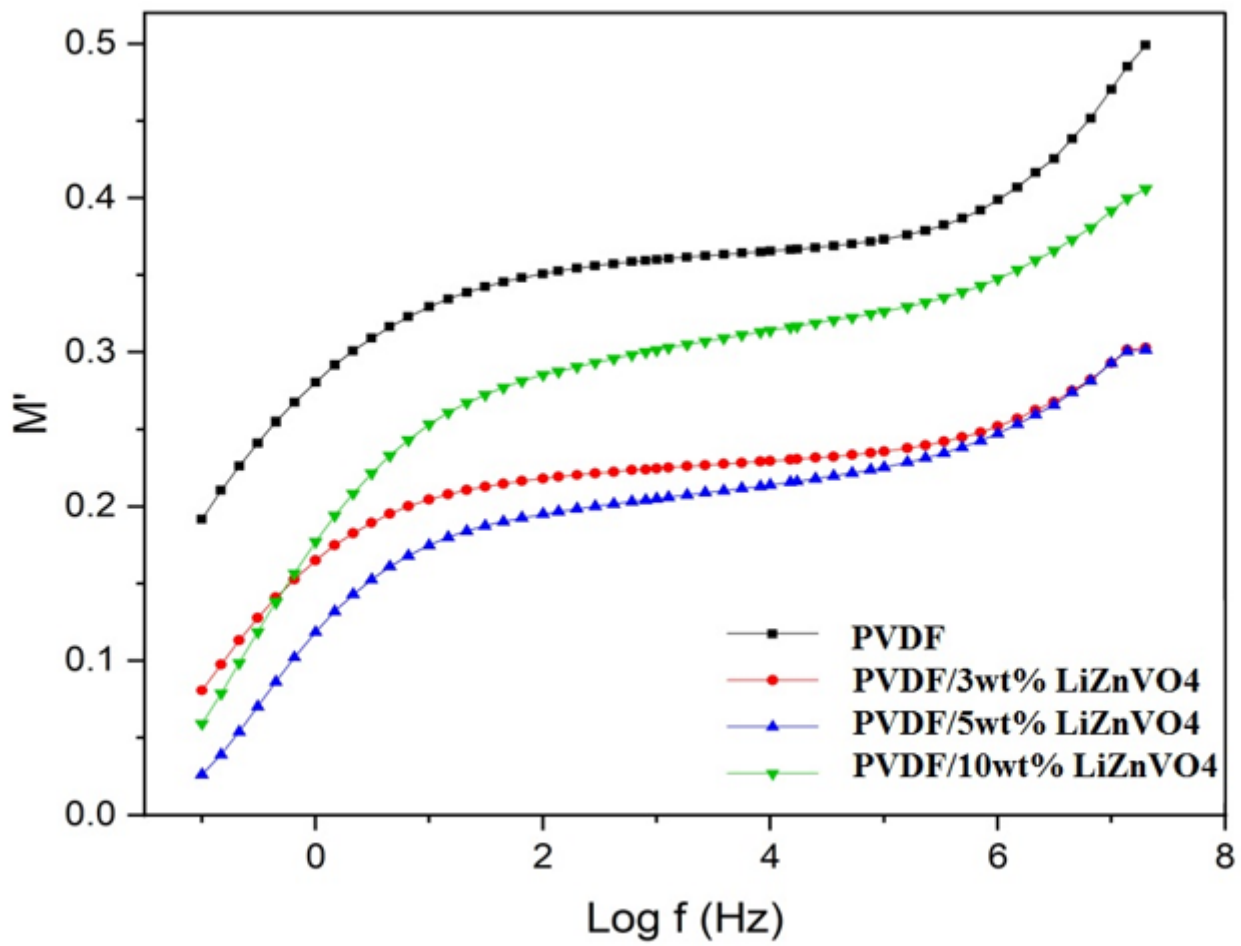


Figure 9

The dependence of M' values on the frequency at 30 °C for PVDF and PVDF doped with a different weight percentage of LiZnVO_4 samples.

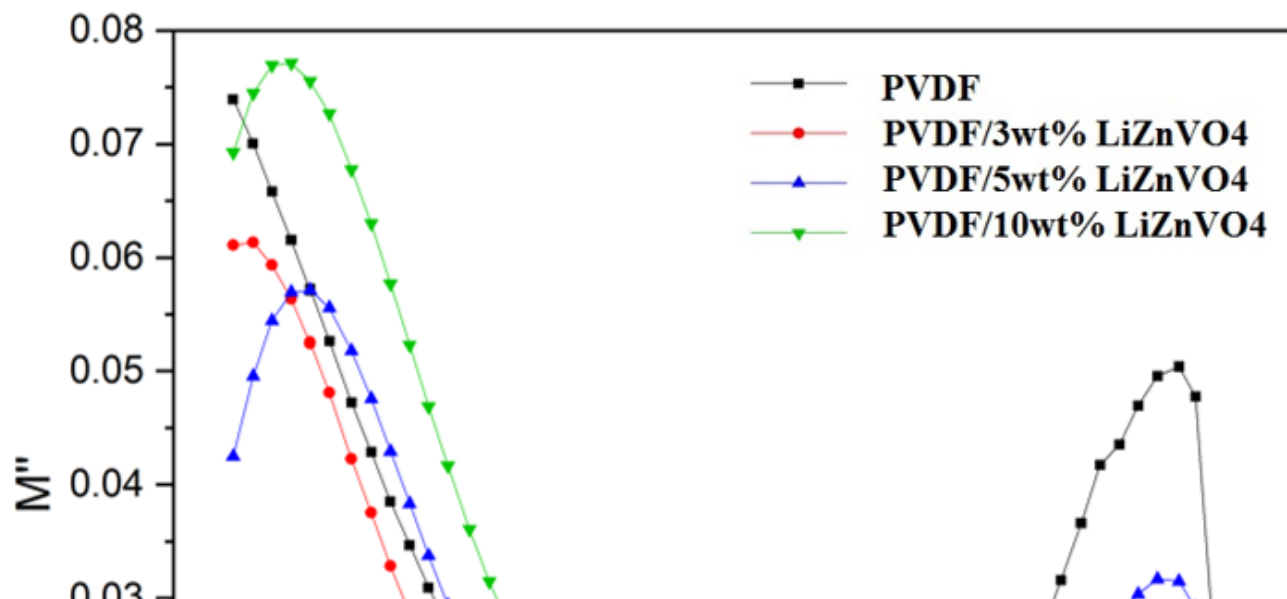


Figure 10

The dependence of M'' values on the frequency at 30 °C for PVDF and PVDF doped with a different weight percentage of LiZnVO_4 samples.

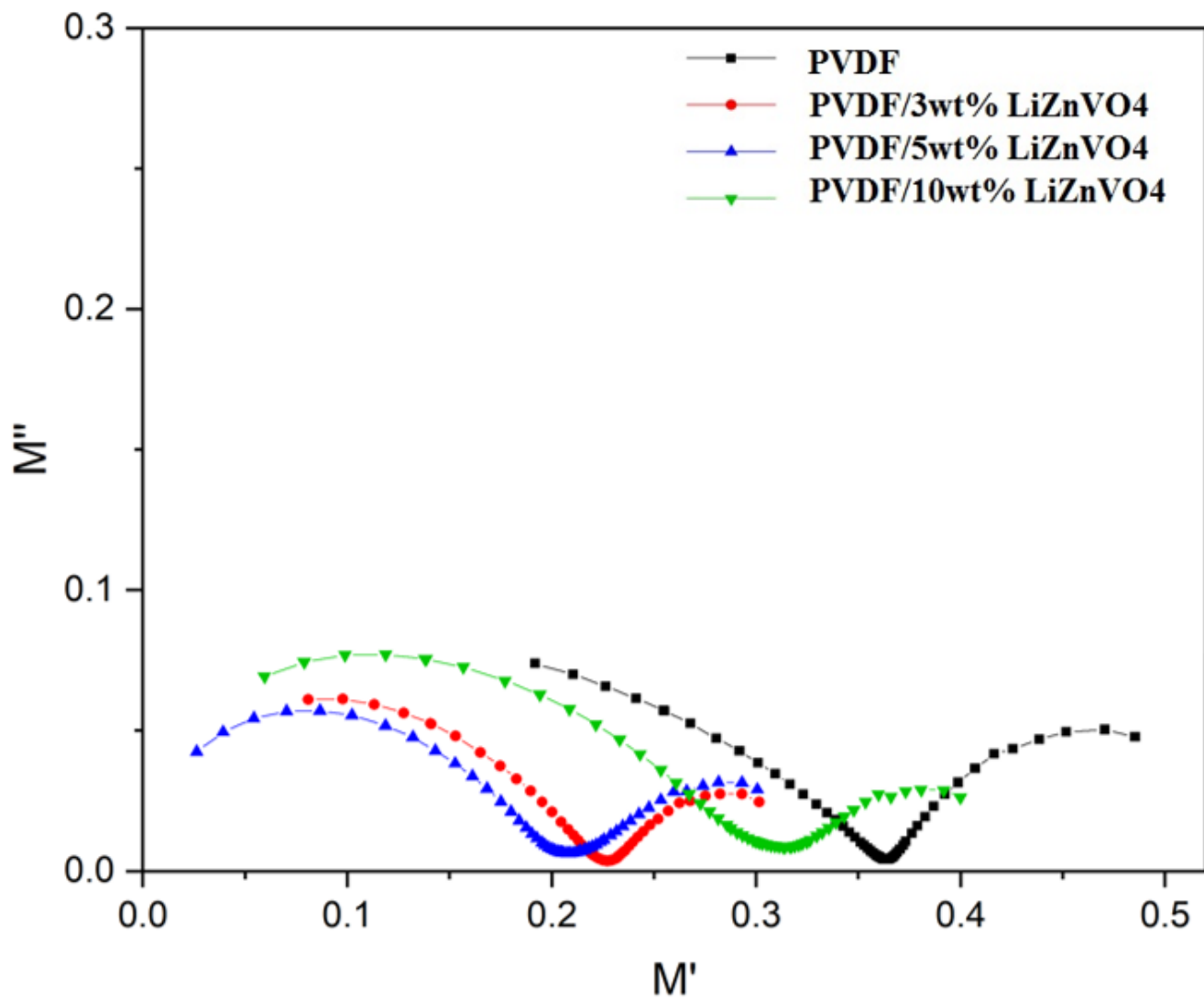


Figure 11

The variation of M'' versus M' at 30 °C for PVDF and PVDF doped with a different weight percentage of LiZnVO_4 samples.

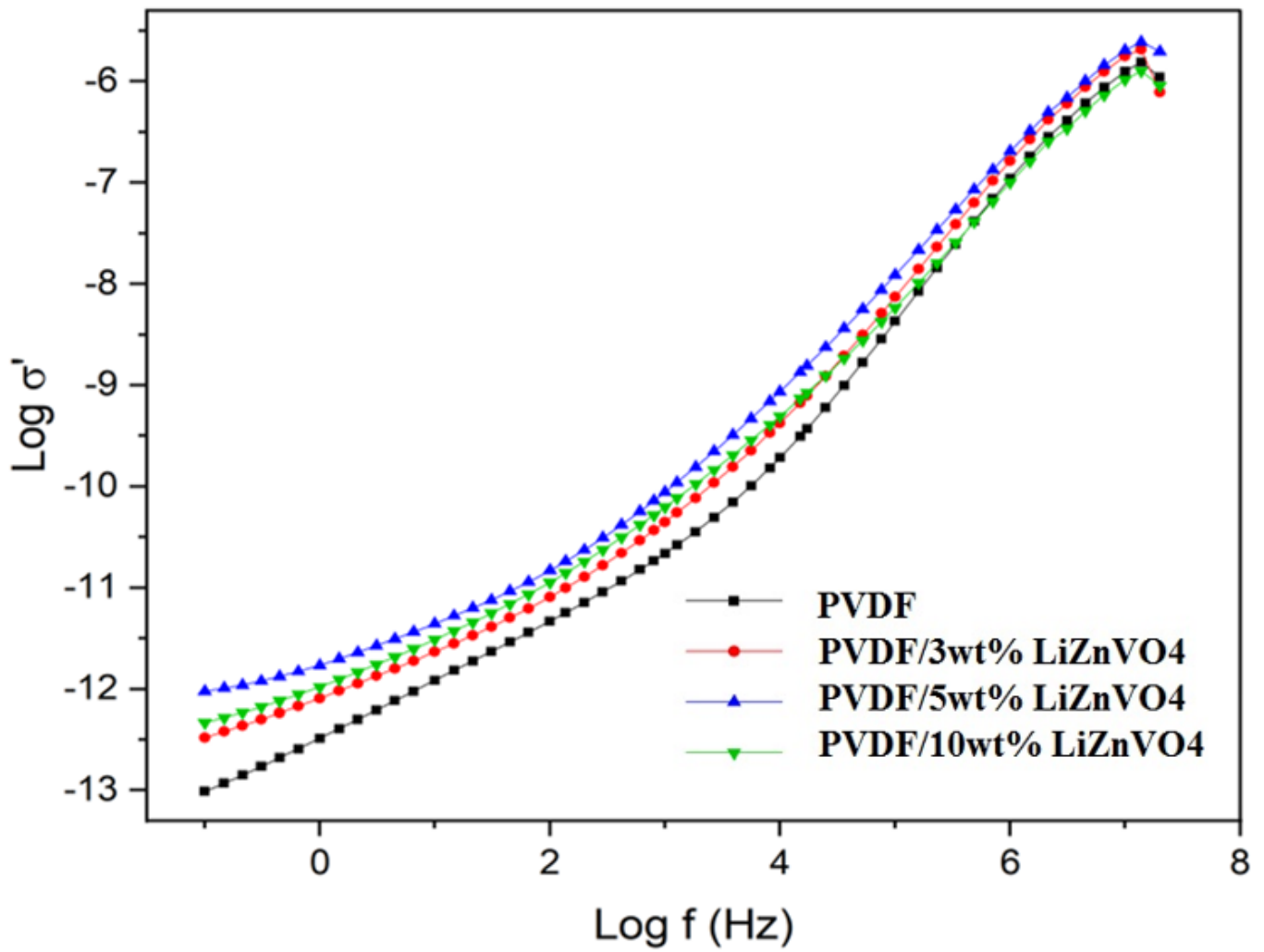


Figure 12

The dependency of AC conductivity (σ_{ac}) on the frequency at 30 °C for PVDF and PVDF doped with a different weight percentage of LiZnVO₄ samples.

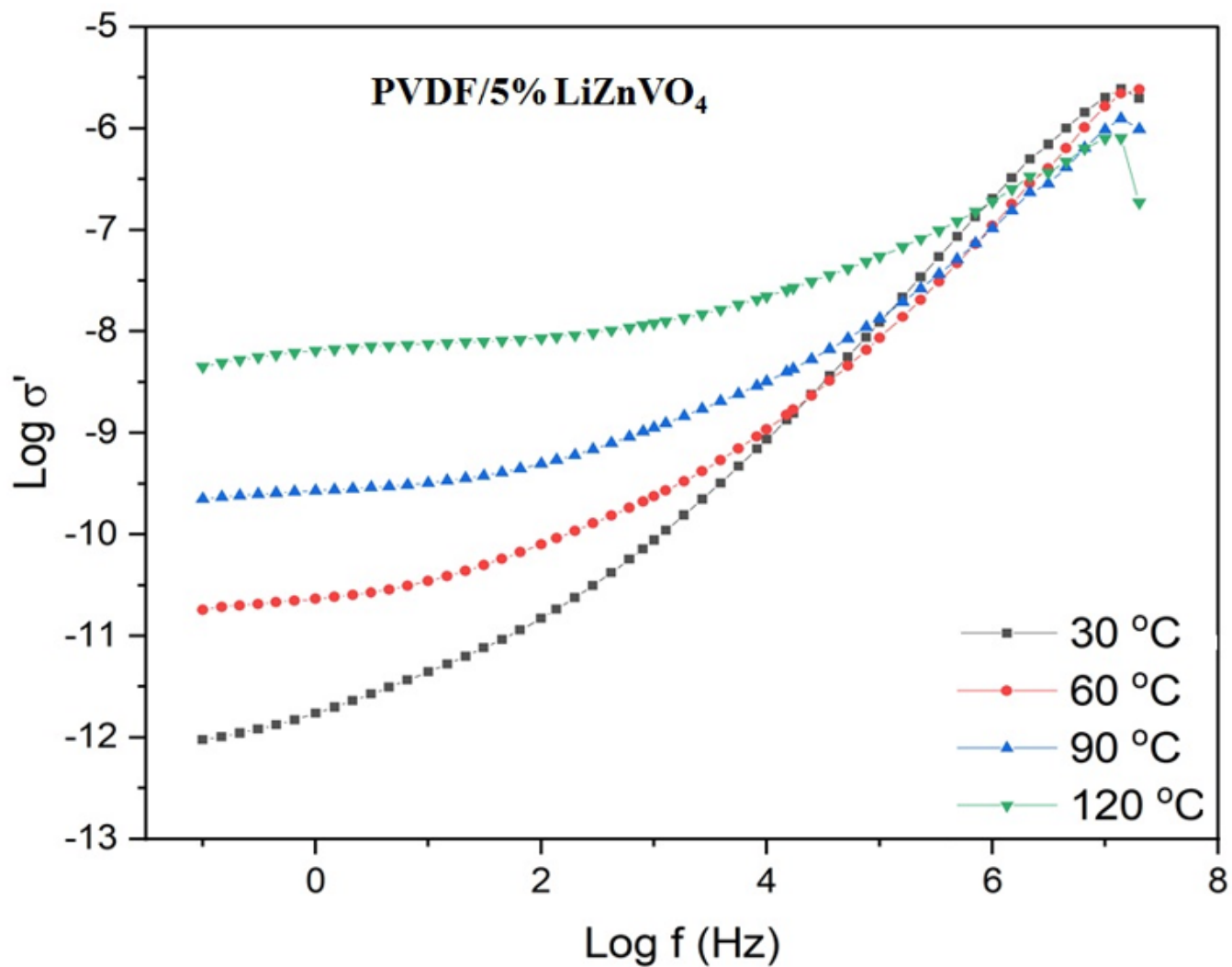


Figure 13

The variation of s_{ac} with frequency curves of the sample containing 5 wt% of LiZnVO₄ (the optimized percentage) at different temperatures.

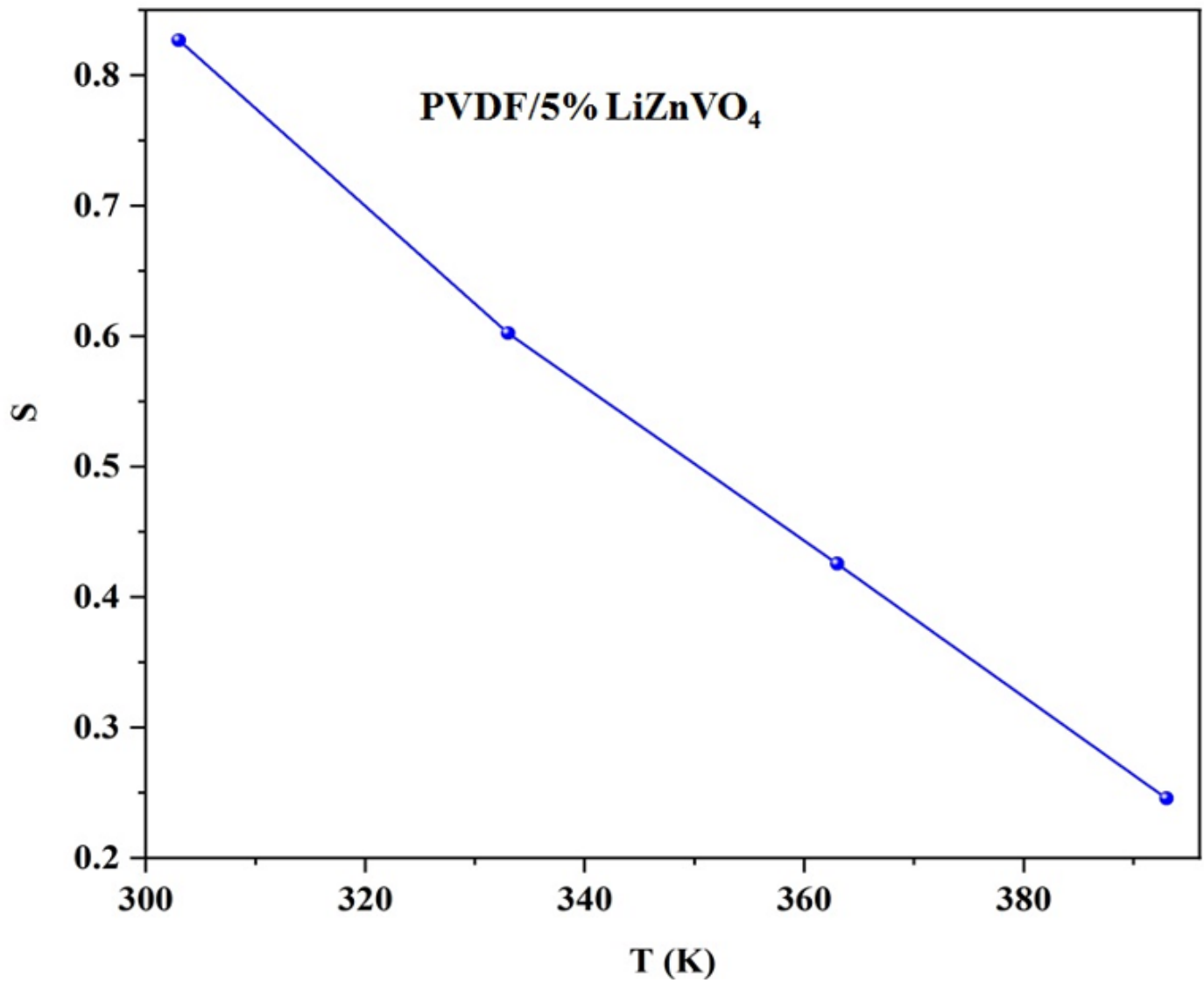


Figure 14

The behavior of S values for the PVDF/5% LiZnVO₄ sample studied in the temperature range 30 °C-120 °C.